Eur. Phys. J. C (2024) 84:1327
https://doi.org/10.1140/epjc/s10052-024-13676-8

THE EUROPEAN PHYSICAL JOURNAL C

Regular Article

Stability of the thin shell from traversable Schwarzschild-like wormholes

Luis Liempi[1,a], **Fabián Orellana**[2,3,b], **Mauricio Cataldo**[4,c]

[1] Departamento de Física, Universidad de Concepción, Casilla 160-C, Concepción, Chile
[2] Centro Interdisciplinario de Neurociencia de Valparaíso (CINV), Universidad de Valparaíso, Valparaíso, Chile Millennium Nucleus in NanoBioPhysics (NNBP), Valparaiso, Chile
[3] Millennium Nucleus in NanoBioPhysics (NNBP), Valparaiso, Chile
[4] Departamento de Física, Universidad del Bío-Bío, Casilla 5-C, Concepción, Chile

Received: 26 August 2024 / Accepted: 2 December 2024

Abstract This article analyses the stability of thin-shell wormholes constructed from non-asymptotically flat wormholes and the vacuum Schwarzschild solution. The construction of these spherically symmetric thin shells focuses on a specific class of wormholes characterized by a shape function that is linearly dependent on the radial coordinate. This introduces angular defects, which can be either deficits or excesses in the solid angle. To analyze the stability of these structures, we employ linear perturbations around a static solution, using a master equation to describe the behavior of stable equilibrium regions. The study is systematically divided to examine both positive and negative surface energy densities, and it delves into various gravitational redshift functions. Finally, it is concluded that the interaction of an external force on the thin shell significantly influences the behaviour of stable regions. It is demonstrated that, in certain cases, the matter supporting the thin shell may be non-exotic, fully satisfying all energy conditions.

1 Introduction

The Einstein field equations predict solutions that have allowed the study of the feasibility of interstellar travel through hypothetical tunnels called wormholes. In 1916, Flamm [1] was the first to describe the form of a wormhole using a coordinate transformation, resulting in what is now known as the Flamm paraboloid. Years later, with the intention of formulating a fundamental theory of particles, Einstein and Rosen [2] find a solution that connected two identical sheets via a bridge. This solution is known as the Einstein–Rosen bridge. In 1955, Wheeler [3], using a geometric approach, postulates the existence of the geon. Two years later, J.A. Wheeler and C.W. Misner study the consequences regarding electric charge, which allows them to visually conceive a wormhole and coin this term in literature [4]. In 1973, Ellis [5] discovers a new solution by coupling a scalar field to the spacetime metric. This traversable wormhole is known as a *drainhole*. Years later, in 1988, Morris and Thorne [6,7], using such solutions as a pedagogical tool to teach Einstein's theory, lay the groundwork for the study of wormholes as a new branch of exotic solutions in general relativity. They find that the matter source supporting wormholes violates all energy conditions; matter with these properties is known as exotic matter.

The theory of singular hypersurfaces and thin shells formulated by Israel [8] has made significant contributions to several areas of gravitation. This theory is based on the study of the extrinsic curvature of a specific spacetime, allowing for a simpler and coordinate-independent treatment to analyze junction conditions. Thus, this method enabled Visser [9,10] to devise a new way to construct spacetime tunnels such as wormholes. The procedure involves cutting out a region of spacetime and matching another spacetime manifold onto it. Visser argues that this technique would allow for the confinement of exotic matter in a finite region of spacetime, enabling a traveler to traverse a thin-shell wormhole without experiencing the effects of exotic matter. Another advantage of this technique is that it permits studying the stability of thin shells, analyzing different equations of state [11,12], or without specifying an equation of state [13–16], extending the analysis to different spacetime symmetries [17,18], and

[a] e-mail: luiliempi@udec.cl (corresponding author)
[b] e-mail: fabian.orellana@postgrado.uv.cl
[c] e-mail: mcataldo@ubiobio.cl

Published online: 28 December 2024

even applying this study to more general theories of gravity [19–23].

In the framework of general relativity, the matter supporting a spacetime geometry must satisfy certain conditions. Typically, these include the requirement that energy density should be positive or dominant over pressures. In the literature, the weak energy condition (WEC) is often invoked. For a homogeneous fluid with energy density ρ and spatially homogeneous pressure p the WEC holds if $\rho \geq 0$ and $\rho + p \geq 0$. By continuity, this implies the null energy condition (NEC), $\rho + p \geq 0$. The strong energy condition (SEC) is satisfied if $\rho + p \geq 0$ and $\rho + 2p \geq 0$, while the dominant energy condition (DEC) holds true if $\rho \geq 0$ and $-\rho \leq p \leq \rho$.

A thin shell in the context of wormholes or other general relativistic structures can be supported by different types of matter depending on the specific configuration of the system. Exotic matter is the most common type of matter considered in thin-shell wormholes. This kind of matter violates the known energy conditions, such as the NEC or WEC, which means it can exhibit negative energy density or pressure.

In the published literature, one can find examples of thin shells supported by matter characterized by an equation of state parameter ω. For $\omega < -1$, the solution is sustained by phantom matter [14]. When $-1 < \omega < -\frac{1}{3}$, the thin shell is supported by dark energy. This type of matter is theoretically required to stabilize the wormhole throat and keep it open.

In this paper, we construct spherically symmetric thin-shell traversable wormhole solutions by matching an interior traversable wormhole solution to an exterior Schwarzschild vacuum spacetime at a junction interface. The interior solution considered is the traversable Schwarzschild-like wormhole constructed in Ref. [24]. This type of solutions is a slight generalization of the traversable Schwarzschild wormhole spacetime, obtained by introducing a linear dependence on the radial coordinate in the shape function. These spacetimes exhibit a solid angle deficit (or excess).

It is important to highlight that thin-shell wormholes supported by non-exotic matter – matter that satisfies the aforementioned energy conditions – have been explored in the literature. In this regard, we can cite solutions with cylindrical symmetry in the context of Brans-Dicke theory [25], as well as solutions with spherical symmetry in the presence of a positive cosmological constant and conformal scalar fields [26].

The interior solution under consideration exhibits either deficits or excesses at infinity, extending the range of asymptotic flatness behaviors found in previously studied wormhole models. The study of geometries with topological defects in general relativity provide essential insights into the physics of high-energy regimes and the past of the universe. One of the most challenging current problems in theoretical physics is explaining the structure formation of the Universe. Particle physics models predict the formation of topological defects during phase transitions in the early universe. Different types of topological objects may have formed during the expansion of the Universe, such as domain walls, cosmic strings, and monopoles [27–29]. Linde proposed that topological defects could serve as seeds for inflation [30]. The study of geometries containing topological defects can also have significant astrophysical implications. Pando et al. [31] proposed that topological defects might play a role in the formation of galactic structures. Nucamendi and collaborators [32–34] further suggested that global monopoles with non-minimal coupling could offer a realistic model for explaining dark matter.

The main goal of this paper is to carry out a stability analysis against spherically symmetric perturbations, linking wormhole stability to the properties of the matter on the thin shell. The presence of solid angle deficits [35–37] or excesses introduces interesting topological features that can have significant implications for the wormhole structure and stability. The solution presented in [24] has been explored across various contexts, including Asymptotically Safe Gravity [38], the Casimir effect [39], and holographic dark energy [40], establishing it as a significant framework for examining thin-shell formation in wormhole spacetimes. Notably, the embedding diagrams for wormholes in [24] differ based on their solid angle characteristics: those with a deficit extend from the throat to infinity, while those with an excess extend from the throat to a maximum radius. Consequently, the shape and size of these wormholes depend on the deficit or excess in solid angle, a characteristic absent in the standard traversable Schwarzschild wormhole spacetime.

In our analysis, we verify that the stability regions can be significantly increased by selecting appropriate choices of the redshift function. Specifically, we consider the cases where the redshift functions are given by $\Phi(r) = 0$, $\Phi(r) = r/r_0$, and $\Phi(r) = r_0/r$.

This paper is organized as follows: In Sect. 2 we outline shortly key aspects related to the Morris and Thorne's traversable wormholes. Section. 3 addresses crucial aspects regarding the construction of thin-shell wormholes by cutting and pasting sections of two distinct manifolds. In Sect. 4 we apply the general formalism described in the previous section to construct wormhole spacetimes. Here, the Schwarzschild-like wormhole serves as the interior solution matched to the exterior vacuum Schwarzschild spacetime at a junction interface. Sections 5 and 6 analyze the equation of state for the thin shell and derive stability regions for the bulk spacetime wormhole, respectively. Section 7 presents our conclusions.

2 Morris–Thorne wormhole spacetimes

We will begin by summarizing key aspects related to the Morris and Thorne traversable wormholes. These authors proposed the following spherically symmetric metric for constructing wormholes:

$$ds^2 = -e^{2\Phi(r)}dt^2 + \frac{dr^2}{1-\frac{b(r)}{r}} + r^2\left(d\theta^2 + \sin^2\theta d\phi^2\right), \tag{1}$$

where $\Phi(r)$ and $b(r)$ are the *redshift* and shape functions, respectively. Additionally, Morris and Thorne discussed the minimal requirements that must be satisfied to obtain a wormhole:

1. The shape function must satisfy $1 - b/r \geq 0$, equality holding for a minimum radius r_0 where the throat of the wormhole is located, i.e., $b(r_0) = r_0$.
2. The redshift function $\Phi(r)$ must remain finite throughout spacetime to ensure the absence of horizons and singularities, thereby achieving a traversable wormhole.
3. The flare-out condition, $\left(b - b'r\right)/2b^2 > 0$, must be maintained to preserve the shape of the wormhole.

Morris and Thorne specifically studied asymptotically flat wormholes. Such solutions connect two regions within the same universe or different universes. For this class of wormholes, an additional condition must be imposed: the shape function must satisfy $b/r \to 0$ as $r \to \infty$.

Considering the metric (1) and an anisotropic energy-momentum tensor $T_{\mu\nu} = diag\left(-\rho,\ p_r,\ p_l,\ p_l\right)$ supporting these wormholes, components of the Einstein field equations are given by

$$\kappa\rho(r) = \frac{b'}{r^2}, \tag{2}$$

$$\kappa p_r(r) = 2\left(1-\frac{b}{r}\right)\frac{\Phi'}{r} - \frac{b}{r^3}, \tag{3}$$

$$\kappa p_l(r) = \left(1-\frac{b}{r}\right)\left[\Phi'' + \Phi'^2 - \frac{b'r+b-2r}{2r(r-b)}\Phi' - \frac{b'r-b}{2r^2(r-b)}\right], \tag{4}$$

where primes denote $\partial/\partial r$, $\rho(r)$ is the energy density, $p_r(r)$ is the radial pressure, and $p_l(r)$ is the lateral pressure measured in the direction orthogonal to the radial direction.

3 Formalism of hypersurfaces and equations of thin-shell wormholes

Let us now outline crucial aspects concerning thin shells, based on the general theoretical analysis performed in [16]. To construct thin-shell wormholes, we must cut and paste sections of two distinct manifolds at a timelike hypersurface Σ, which we denote as the outer region $\mathcal{M}_+$ and the inner region $\mathcal{M}_-$ [10–23]. Subsequently, these manifolds must be joined in such a way that we obtain the complete manifold, $\mathcal{M} = \mathcal{M}_+ \cup \mathcal{M}_-$, namely, a geodesically complete spacetime. In other words, this single manifold $\mathcal{M}$ is obtained by gluing together the two distinct manifolds $\mathcal{M}_+$ and $\mathcal{M}_-$, at their boundaries, which are given by Σ_+ and Σ_-, respectively. This leads us to the identification of their boundaries, such that the hypersurfaces where the junction occurs must satisfy $\Sigma_+ = \Sigma_- = \Sigma$. The induced metrics on the hypersurfaces Σ_+ and Σ_- must also satisfy $g^+_{ij} = g^-_{ij} = g_{ij}$, meaning that if we take the coordinates $\xi^i = \xi^i(\tau, \theta, \phi)$ intrinsic to the hypersurface, these remain invariant under isometric transformations $g^+_{ij}(\xi) = g^-_{ij}(\xi) = g_{ij}(\xi)$. Moreover, if $g^+_{\mu\nu}(x^\mu_+)$ and $g^-_{\mu\nu}(x^\mu_-)$ are the metrics of $\mathcal{M}_+$ and $\mathcal{M}_-$, respectively, then the first fundamental form of the junction hypersurface Σ is given by $g_{ij} = g_{\mu\nu}e^\mu_{(i)}e^\nu_{(j)}|_\pm$, hence its intrinsic metric is given by

$$ds^2_\Sigma = -d\tau^2 + a(\tau)^2\left(d\theta^2 + \sin^2\theta\, d\phi^2\right), \tag{5}$$

where $a(\tau)$ is the radius of the thin shell and τ is the proper time of an observer comoving with the junction surface.

The junction hypersurface is defined by the parametric equation $f(x^\mu(\xi^i)) = 0$ and its position is described by $x^\mu(\tau, \theta, \phi) = (t(\tau), a(\tau), \theta, \phi)$. The expression for the four-velocities, measured in the static coordinate systems on both sides of the hypersurface, is given by

$$u^\mu_\pm = \frac{dx^\mu}{d\tau} = (\dot{t}, \dot{a}, 0, 0), \tag{6}$$

where the dots denote derivatives with respect to τ.

According to the formalism of Israel [8], the unit normal vector n_μ must be oriented from $\mathcal{M}_-$ to $\mathcal{M}_+$ and is defined as

$$n_\mu = \pm\sqrt{\left|g^{\alpha\beta}\frac{\partial f}{\partial x^\alpha}\frac{\partial f}{\partial x^\beta}\right|^{-1}}\frac{\partial f}{\partial x^\mu}. \tag{7}$$

The extrinsic curvature or second fundamental form is defined as $K_{ij} = n_{\mu;\nu}e^\mu_{(i)}e^\nu_{(j)}$. Differentiating $n_\mu e^\mu_{(i)} = 0$ with respect to ξ^j, we obtain

$$n_\mu\frac{\partial^2 x^\mu}{\partial\xi^i\partial\xi^j} = -n_{\mu,\nu}\frac{\partial x^\mu}{\partial\xi^i}\frac{\partial x^\nu}{\partial\xi^j}. \tag{8}$$

Using the covariant derivative of n_μ in Eq. (8), we obtain for the extrinsic curvature the expression

$$K_{ij}^{\pm} = -n_\mu \left(\frac{\partial^2 x^\mu}{\partial\xi^i \partial\xi^j} + \Gamma^{\mu\pm}_{\alpha\beta} \frac{\partial x^\mu}{\partial\xi^i} \frac{\partial x^\nu}{\partial\xi^j} \right). \tag{9}$$

For the discontinuity of K_{ij} on the hypersurface Σ, we use the following notation

$$\kappa_{ij} = K_{ij}^{+} - K_{ij}^{-}. \tag{10}$$

From the Lanczos equations, the components of the induced stress-energy tensor on the hypersurface are given by

$$S^i{}_j = -\frac{1}{8\pi} \left(\kappa^i{}_j + \delta^i{}_j \kappa^k{}_k \right). \tag{11}$$

Due to spherical symmetry of the junction hypersurface, considerable simplifications occur, namely

$$\kappa^i{}_j = \mathrm{diag}\left(\kappa^\tau{}_\tau, \kappa^\theta{}_\theta, \kappa^\phi{}_\phi \right). \tag{12}$$

The stress-energy tensor can be written in terms of the surface energy density σ and the surface pressure $\mathcal{P}$, as

$$S^i{}_j = \mathrm{diag}\left(-\sigma, \mathcal{P}, \mathcal{P} \right). \tag{13}$$

In addition, the Lanczos equations provide us with a balance equation on the shell through

$$S^i{}_{j|i} = \left[T_{\mu\nu} e^\mu_{(j)} n^\nu \right]^{+}_{-}. \tag{14}$$

Now on, we shall consider two generic static spherically symmetric spacetimes given by the following line elements:

$$ds^2 = -e^{2\Phi_\pm(r_\pm)} dt_\pm^2 + \frac{dr_\pm^2}{1 - \frac{b_\pm(r_\pm)}{r_\pm}} + r_\pm^2 \left(d\theta_\pm^2 + \sin^2\theta_\pm d\phi_\pm^2 \right), \tag{15}$$

which clearly are related to the metric (1). In this case the signs + and − correspond to spacetime manifolds $\mathcal{M}_+$ and $\mathcal{M}_-$, respectively. Then, the matching occurs at $f(r,\tau) = r - a(\tau) = 0$, where $a(\tau)$ is the radius of the hypersurface.

For the metric (15), the normal vector is given by

$$n_\mu^\pm = \left(-\frac{e^{\Phi_\pm(a)}}{\sqrt{1 - \frac{b_\pm(a)}{a}}} \dot{a}, \frac{\sqrt{\dot{a}^2 + 1 - \frac{b_\pm(a)}{a}}}{1 - \frac{b_\pm(a)}{a}}, 0, 0 \right), \tag{16}$$

where the overdot indicates differentiation with respect to τ. The non-trivial components of the extrinsic curvature can be directly computed as

$$K^{\tau\pm}{}_\tau = \frac{\Phi'_\pm(a) \left(\dot{a}^2 + 1 - \frac{b_\pm(a)}{a} \right) + \ddot{a} - \frac{\dot{a}^2 \left(b_\pm(a) - a b'_\pm(a) \right)}{2a(a - b_\pm(a))}}{\sqrt{\dot{a}^2 + 1 - \frac{b_\pm(a)}{a}}}, \tag{17}$$

$$K^{\theta\pm}{}_\theta = \pm \frac{1}{a} \sqrt{\dot{a}^2 + 1 - \frac{b_\pm(a)}{a}}, \tag{18}$$

where the prime now denotes a derivative with respect to the coordinate a.

Then, using Eqs. (10) and (11), we can compute the components of the thin shell stress-energy tensor

$$\sigma = -\frac{1}{4\pi a} \left[\sqrt{\dot{a}^2 + 1 - \frac{b_+(a)}{a}} - \sqrt{\dot{a}^2 + 1 - \frac{b_-(a)}{a}} \right], \tag{19}$$

$$\mathcal{P} = \frac{1}{8\pi a} \times \left[\frac{\left(a\Phi'_+(a) + 1 \right) \left(\dot{a}^2 + 1 - \frac{b_+(a)}{a} \right) + a\ddot{a} - \frac{\dot{a}^2 \left(b_+(a) - a b'_+(a) \right)}{2(a - b_+(a))}}{\sqrt{\dot{a}^2 + 1 - \frac{b_+(a)}{a}}} - \frac{\left(a\Phi'_-(a) + 1 \right) \left(\dot{a}^2 + 1 - \frac{b_-(a)}{a} \right) + a\ddot{a} - \frac{\dot{a}^2 \left(b_-(a) - a b'_-(a) \right)}{2(a - b_-(a))}}{\sqrt{\dot{a}^2 + 1 - \frac{b_-(a)}{a}}} \right], \tag{20}$$

where σ and $\mathcal{P}$ are the surface energy density and the tangential surface pressure, respectively. From these equations, it follows that when $b_+(a) = b_-(a)$ and $\Phi_+(a) = \Phi_-(a)$, the components of the stress-energy tensor (13) vanish. The mass of the thin shell can be written as $m_s(a) = 4\pi a^2 \sigma(a)$. By using Eq. (19), we find

$$m_s(a) = -a \left(\sqrt{\dot{a}^2 + 1 - \frac{b_+(a)}{a}} - \sqrt{\dot{a}^2 + 1 - \frac{b_-(a)}{a}} \right). \tag{21}$$

Notably, both this expression and Eq. (19) can assume positive or negative values depending on the shape functions $b_+(a)$ and $b_-(a)$. Equation (21) will subsequently be used to derive the equation of motion for the thin shell, a key component in the stability analysis.

Furthermore, for our goal of analyzing the stability of thin shells, we consider Eq. (14), from which we obtain the energy balance equation of the thin shell

$$\dot{\sigma} + \frac{2(\sigma + \mathcal{P})}{a} \dot{a} = \Xi \dot{a}, \tag{22}$$

where

$$\Xi = \frac{1}{4\pi a^2} \left[\left(a\Phi'_+(a) + \frac{a b'_+(a) - b_+(a)}{2(a - b_+(a))} \right) \sqrt{\dot{a}^2 + 1 - \frac{b_+(a)}{a}} - \left(a\Phi'_-(a) + \frac{a b'_-(a) - b_-(a)}{2(a - b_-(a))} \right) \sqrt{\dot{a}^2 + 1 - \frac{b_-(a)}{a}} \right]. \tag{23}$$

On the left-hand side of Eq. (22), we have the variation of the internal energy of the shell and the work done by the internal force of the shell itself, and on the right-hand side, we have the term corresponding to the work done by external forces on the shell. More specifically, Ξ arises due to a discontinuity in the shell and is interpreted as a flux of momentum across the thin shell. From Eq. (23), we note that $\Phi_+(a) = \Phi_-(a) = 0$ does not necessarily imply $\Xi = 0$. This will depend on the form of the shape functions $b_+(a)$ and $b_-(a)$.

3.1 Static linearized equation of motion

Now, we shall consider a linearization around an assumed static solution. From Eq. (21), we deduce the thin shell equation of motion given by

$$\dot{a}^2 + V(a) = 0, \tag{24}$$

where the potential $V(a)$ takes the form

$$V(a) = F_1(a) - \left[\frac{m_s(a)}{2a}\right]^2 - \left[\frac{F_2(a)}{m_s(a)}\right]^2, \tag{25}$$

this equation is in terms of the thin shell mass $m_s(a) = 4\pi a^2\sigma(a)$ and the functions

$$F_1(a) = 1 - \frac{b_+(a) + b_-(a)}{2a}, \tag{26}$$

$$F_2(a) = \frac{b_+(a) - b_-(a)}{2}. \tag{27}$$

We consider a linearization around a static solution a_0 of the thin-shell equation of motion, which also implies a solution $\ddot{a} = V'(a)$. Consequently, $m_s(a_0) = 4\pi a^2\sigma(a_0)$, where

$$m_s(a_0) = -a_0\left(\sqrt{1 - \frac{b_+(a_0)}{a_0}} - \sqrt{1 - \frac{b_-(a_0)}{a_0}}\right). \tag{28}$$

From the equation of motion Eq. (24),

$$\dot{a}^2 + V(a) = 0 \;\Rightarrow\; \dot{a}^2 = -V(a).$$

Expanding the potential $V(a)$ in a Taylor series up to second order around the solution a_0,

$$V(a) = V(a_0) + V'(a_0)(a - a_0) + \frac{1}{2}V''(a_0)(a - a_0)^2 + O((a - a_0)^3).$$

Furthermore, around the static solution $\dot{a}_0 = \ddot{a}_0 = 0$, we have the conditions $V(a_0) = V'(a_0) = 0$, so we only need to consider

$$V(a) = \frac{1}{2}V''(a_0)(a - a_0)^2.$$

Using Eq. (25), the first and second derivatives of $V(a)$ are

$$V'(a) = F_1' - 2\left(\frac{m_s}{2a}\right)\left(\frac{m_s}{2a}\right)' - 2\left(\frac{F_2}{m_s}\right)\left(\frac{F_2}{m_s}\right)', \tag{29}$$

$$V''(a) = F_1'' - 2\left[\left(\frac{m_s}{2a}\right)'\right]^2 - 2\left(\frac{m_s}{2a}\right)\left(\frac{m_s}{2a}\right)'' - 2\left[\left(\frac{F_2}{m_s}\right)'\right]^2 - 2\left(\frac{F_2}{m_s}\right)\left(\frac{F_2}{m_s}\right)''. \tag{30}$$

Since $V'(a_0) = 0$, we rewrite it as

$$\left(\frac{m_s}{2a_0}\right)' \equiv \Gamma = \left(\frac{a_0}{m_s}\right)\left[F_1' - 2\left(\frac{F2}{m_s}\right)\left(\frac{F2}{m_s}\right)'\right]. \tag{31}$$

A stable solution exists only if a_0 is a local minimum of $V(a_0)$ and if the second derivative of the potential is greater than zero, i.e., $V''(a_0) > 0$. From Eqs. (30) and (31), we find the expression

$$\left(\frac{m_s}{2a_0}\right)\left(\frac{m_s}{2a_0}\right)'' < \Psi - \Gamma^2, \tag{32}$$

where Ψ is defined as

$$\Psi = -\frac{F_1''}{2} - \left[\left(\frac{F_2}{m_s}\right)'\right]^2 - \left(\frac{F_2}{m_s}\right)\left(\frac{F_2}{m_s}\right)''. \tag{33}$$

The assumed static solution at a_0 is stable if and only if $V(a)$ has a local minimum at a_0, which requires $V''(a_0) > 0$.

3.2 Master equation

Now, we can deduce a master equation that dictates the stable equilibrium configurations [15]. To do this, let us first rewrite Eq. (22) by using $\frac{\dot{\sigma}}{\dot{a}} = \frac{d\sigma}{da} = \sigma'$. Then, we obtain

$$\sigma' = -\frac{2}{a}(\sigma + \mathcal{P}) + \Xi, \tag{34}$$

and its second derivative

$$\sigma'' = \frac{6}{a^2}(\sigma + \mathcal{P}) - \frac{2}{a}\Xi - \frac{2}{a}(\sigma'\eta) + \Xi', \tag{35}$$

where we have defined the parameter

$$\eta = \frac{\mathcal{P}'}{\sigma'} = \frac{d\mathcal{P}}{d\sigma}, \tag{36}$$

which relates the variation of the tangential surface pressure to the variation of surface energy density in the thin shell.

That is, it is linked to the equation of state of the shell. In the literature, this parameter is interpreted as the square of the speed of sound in the thin shell. Rewriting Eq. (35) in terms of the surface mass of the shell $m_s(a_0) = 4\pi a^2\sigma(a_0)$, evaluated at the static solution a_0 we obtain

$$\left(\frac{m_s}{2a_0}\right)'' = \Upsilon - 4\pi\sigma'\eta_0, \tag{37}$$

where

$$\Upsilon = \frac{4\pi}{a_0}(\sigma + \mathcal{P}) + 2\pi a_0 \Xi'. \tag{38}$$

Notice that Eq. (37) explicitly includes the parameter η_0, which will be used to analyze the stability regions of the thin shell.

Now, substituting Eq. (37) into (32), and solving for the parameter η_0 at the static solution a_0, we find the master equation that allows us to study the stability regions of the thin shell

$$\eta_0 = \eta(a_0) > \frac{1}{m_s \sigma'}\left(-\frac{a_0}{2\pi}(\Psi - \Gamma^2) + \frac{m_s \Upsilon}{4\pi}\right), \tag{39}$$

The solutions to the Eq. (39) are

$$\eta_0 > \Lambda_0, \quad \text{if} \quad m_s\sigma' > 0, \tag{40}$$

$$\eta_0 < \Lambda_0, \quad \text{if} \quad m_s\sigma' < 0, \tag{41}$$

where

$$\Lambda_0 = \Lambda(a_0) \equiv \frac{-\frac{a_0}{2\pi}(\Psi - \Gamma^2) + \frac{m_s \Upsilon}{4\pi}}{m_s \sigma'}. \tag{42}$$

This expression characterizes the stability regions of the metric (15). Furthermore, it reveals that both the surface mass m_s and the derivative of the surface energy density σ' play a crucial role in determining the stability intervals of the thin shell. A graphical analysis of Eq. (42) will be presented in Sect. 6.

4 Thin shell with Schwarzschild-like interior wormhole

In this section, we will apply the described general formalism to a specific wormhole spacetime and derive its corresponding stability regions. Specifically, we will construct wormhole solutions by matching an interior traversable wormhole solution to the exterior vacuum Schwarzschild spacetime at a junction interface. In such a way, our approach considers as exterior solution the Schwarzschild metric

$$ds^2 = -\left(1 - \frac{2M}{r_+}\right)dt_+^2 + \frac{dr_+^2}{\left(1 - \frac{2M}{r_+}\right)} + r_+^2\left(d\theta_+^2 + \sin^2\theta_+ d\phi_+^2\right), \tag{43}$$

while as the interior solution the Schwarzschild-like wormhole studied in [24]. This solution is obtained by imposing a linear behavior on the radial coordinate in the shape function $b_-(r_-)$ given by

$$b_-(r_-) = (1-\beta)\, r_0 + \beta r_-. \tag{44}$$

Subsequently, the metric (15) takes the form

$$ds^2 = -e^{2\Phi(r)}dt^2 + \frac{dr^2}{(1-\beta)\left(1 - \frac{r_0}{r}\right)} + r^2\left(d\theta^2 + \sin^2\theta d\phi^2\right), \tag{45}$$

where we have dropped the $-$ subscript to avoid overloading the notation for the interior solution (45). Using the Einstein field equation for the metric (45), the stress-energy tensor components are given by

$$\kappa\rho(r) = \frac{\beta}{r^2}, \tag{46}$$

$$\kappa p_r(r) = 2(1-\beta)\left(1 - \frac{r_0}{r}\right)\frac{\Phi'}{r} - \frac{(1-\beta)r_0 + \beta r}{r^3}, \tag{47}$$

$$\kappa p_l(r) = (1-\beta) \times \left[\left(1 - \frac{r_0}{r}\right)\Phi'' + \left(r\Phi' + 1\right)\left(\left(1 - \frac{r_0}{r}\right)\frac{\Phi'}{r} + \frac{r_0}{2r^3}\right)\right]. \tag{48}$$

Notice that the parameter β, to maintain the Lorentzian nature of the metric (45), must be restricted to $\beta < 1$. Additionally, we note that the spacetime described by this metric exhibits at spatial infinity a solid angle deficit for $0 < \beta < 1$ and a surplus for $\beta < 0$.

The joining hypersurface of both solutions corresponds to the thin shell, which has a radius a_0 and a surface area given by $A = 4\pi a_0^2$.

To avoid for the exterior solution the event horizon, the thin shell radius must satisfy $r_+ = a_0 > 2M$. Now, using equations (19) and (20), we obtain the following components of the energy-momentum tensor of the thin shell

$$\sigma = -\frac{1}{4\pi a_0}\left[\sqrt{1 - \frac{2M}{a_0}} - \sqrt{(1-\beta)\left(1 - \frac{r_0}{a_0}\right)}\right], \tag{49}$$

$$\mathcal{P} = \frac{1}{8\pi a_0}\left[\frac{1 - \frac{M}{a_0}}{\sqrt{1 - \frac{2M}{a_0}}} - \left(a_0\Phi' + 1\right)\sqrt{(1-\beta)\left(1 - \frac{r_0}{a_0}\right)}\right], \tag{50}$$

where σ and $\mathcal{P}$ are the surface energy density and the tangential surface pressure, respectively.

The surface mass and the derivative of the energy density of the shell are given by

$$m_s(a_0) = -a_0\left[\sqrt{1 - \frac{2M}{a_0}} - \sqrt{(1-\beta)\left(1 - \frac{r_0}{a_0}\right)}\right], \tag{51}$$

$$\sigma' = \frac{1}{4\pi a_0^2}\left[\frac{1 - \frac{3M}{a_0}}{\sqrt{1 - \frac{2M}{a_0}}} - \frac{(1-\beta)\left(a_0 - \frac{3r_0}{2}\right)}{a_0\sqrt{(1-\beta)\left(1 - \frac{r_0}{a_0}\right)}}\right]. \tag{52}$$

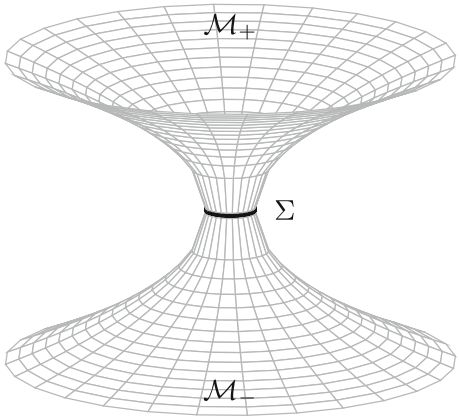

Fig. 1 The figure depicts an embedding diagram of the constructed traversable thin-shell wormhole. The single manifold is obtained by gluing together the vacuum Schwarzschild solution $\mathcal{M}_+$ and the Schwarzschild-like wormhole solution $\mathcal{M}_-$ at the junction surface Σ, joined at a radial coordinate a_0, which represents the thin shell. The surface stress-energy tensor on Σ is given in terms of the surface energy density (49), and the surface pressure (50)

Additionally, there is a momentum flux term acting on the shell given by

$$\Xi(a_0) = \frac{\left(\frac{r_0}{2} - a_0\,(a_0 - r_0)\,\Phi'\right)\sqrt{(1-\beta)\left(1-\frac{r_0}{a_0}\right)}}{4\pi a^2\,(a_0 - r_0)}. \tag{53}$$

We conclude from this equation that the momentum flux depends explicitly on $\Phi(r)$, as well as on the deficit or excess of the solid angle $1-\beta$.

It should be noted that certain cases where there is neither a deficit nor an excess in solid angle (i.e. $\beta = 0$) for the interior solution (45) have been studied previously in the literature. When the β-parameter vanishes, the following cases may be considered: (i) for $e^{2\Phi(r)} = 1 - \frac{2M}{r}$ and $r_0 = 2\,M$, the interior and exterior manifolds are given by the schwarzschild spacetime (43); (ii) for $b(r) = r_0$ wormhole solutions characterized by the redshift functions $\Phi(r) = 0$ and $\Phi(r) = \frac{r_0}{r}$ can be constructed. These solutions can be matched to exterior Schwarzschild spacetime. These three cases of spherically symmetric solutions were discussed in [15].

A three-dimensional embedding diagram of the gluing of this solution with the Schwarzschild metric is shown in Fig. 1.

5 Analysis of equation of state of the thin shell

It is also interesting to analyse the equation of state for the thin shell $\omega = \frac{\mathcal{P}}{\sigma}$ obtained from Eqs.(49) and (50). For simplicity, we consider the zero-tidal-force solution. Then, for $\Phi(r) = 0$, Eqs. (49) and (50) imply that

$$\omega = -\frac{1}{2}\left[\frac{\frac{1-\frac{M}{a_0}}{\sqrt{1-\frac{2M}{a_0}}} - \sqrt{(1-\beta)\left(1-\frac{r_0}{a_0}\right)}}{\sqrt{1-\frac{2M}{a_0}} - \sqrt{(1-\beta)\left(1-\frac{r_0}{a_0}\right)}}\right]. \tag{54}$$

Let us first analyse the case $\beta = 0$. From Eq. (54), we deduce that in the asymptotic limit as $a_0 \to \infty$, the state parameter approaches $\omega = -1/2$, implying that the thin shell is supported by dark energy. More specifically, the state parameter is associated with quintessence cosmological models, where ω ranges from $-1 \leq \omega \leq -1/3$.

Let us now consider cases with non vanishing values of the β-parameter. From Eq. (54), we observe that the thin shell can be supported by dark energy and phantom matter in the following cases:

1. For $\beta < 0$:
   - Dark energy:
     (a) For $r_0 < 2M$, then $\zeta_1 + \zeta_2 < a_0$.
     (b) For $3M < r_0$, then
        i. $r_0 < a_0 < \zeta_3 + \zeta_4$ and
        ii. $\zeta_1 + \zeta_2 < a_0$.
     (c) For $\frac{r_0}{3} \leq M < \frac{r_0}{2}$, then $\zeta_1 + \zeta_2 < a_0$.
   - Phantom matter:
     (a) For $2M < r_0$, then $r_0 < a_0 < \frac{2M - r_0(1-\beta)}{\beta}$.
2. For $0 < \beta < 1$:
   - Dark energy:
     (a) For $r_0 < 2M$, then $\zeta_3 + \zeta_4 < a_0$.
     (b) For $M \leq \frac{r_0}{4}$, then $r_0 < a_0$.
     (c) For $\frac{r_0}{4} < M < \frac{r_0}{3}$:
        i. $0 < \beta < \frac{(r_0-4M)^2}{(r_0-2M)^2}$, then
        A. $r_0 < a_0 < \zeta_3 - \zeta_4$.
        B. $\zeta_3 + \zeta_4 < a_0$.
        ii. $\beta = \frac{(r_0-4M)^2}{(r_0-2M)^2}$, then $r_0 < a_0$, with $a_0 \neq \zeta_3 - \zeta_4$.
        iii. $\frac{(r_0-4M)^2}{(r_0-2M)^2} < \beta < 1$, then $r_0 < a_0$.
     (d) For $\frac{r_0}{3} \leq M < \frac{r_0}{2}$, then $\zeta_3 + \zeta_4 < a_0$.
   - Phantom matter:
     (a) For $r_0 < 2M$, then $\frac{2M - r_0(1-\beta)}{\beta} < a_0$.
     (b) For $2M < r_0$, then $r_0 < a$.

where

$$\zeta_1 = \frac{2M(\beta-2) - r_0(1-\beta)}{2\beta}, \tag{55}$$

$$\zeta_2 = \frac{1}{2}\sqrt{\frac{(1-\beta)((r_0+4M)^2 - (r_0-2M)^2\beta)}{\beta^2}}, \tag{56}$$

$$\zeta_3 = \frac{2M(\beta+2) - r_0(1-\beta)}{2\beta}, \tag{57}$$

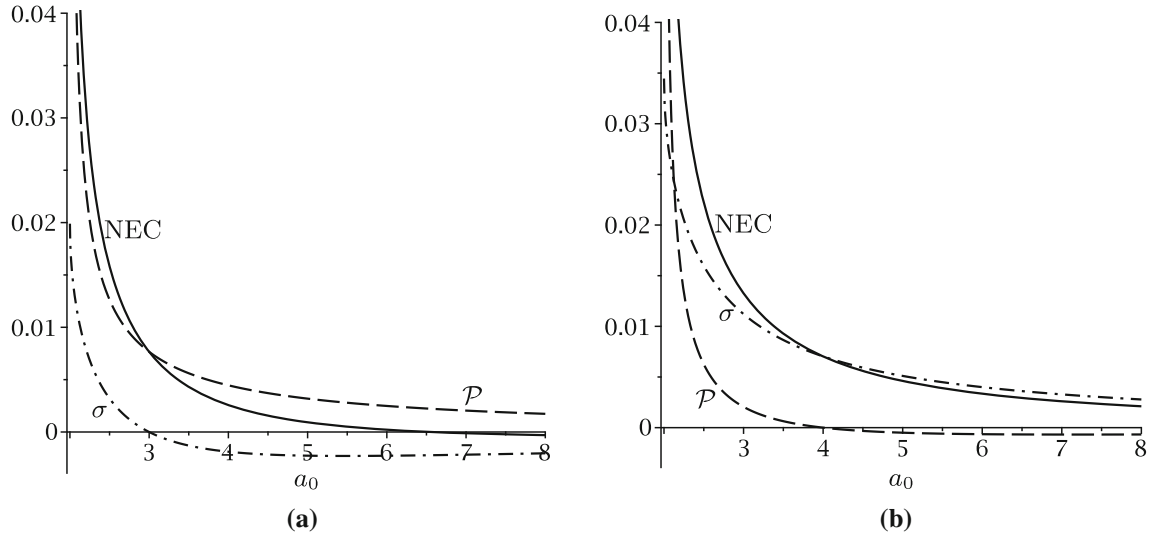

Fig. 2 The behavior of the surface energy density (dash-dot line), surface tangential pressure (dashed line), and NEC (solid line) as functions of the junction radius a_0 is depicted in these plots for the parameter values $2M > r_0$, $\Phi(r) = 0$, and $M = r_0 = 1$. Figure (**a**) shows the case for $\beta = \frac{1}{2}$, while Figure (**b**) illustrates the scenario for $\beta = -\frac{1}{2}$. For details, refer to the text

$$\zeta_4 = \frac{1}{2}\sqrt{\frac{(1-\beta)\left((r_0-4M)^2-(r_0-2M)^2\beta\right)}{\beta^2}}. \tag{58}$$

We can also study certain characteristics of the energy conditions of the thin shell directly using expressions for the surface energy density (49) and the tangential surface pressure (50). We initiate this analysis by first considering NEC, which in general, for an anisotropic fluid is expressed as

$$\sigma + \mathcal{P}_i \geq 0.$$

Taking into account Eqs. (49) and (50) NEC takes the following form

$$\sigma + \mathcal{P} = \frac{1}{8\pi a_0}\left[\frac{\frac{3M}{a_0}-1}{\sqrt{1-\frac{2M}{a_0}}} + \sqrt{(1-\beta)\left(1-\frac{r_0}{a_0}\right)}\right]. \tag{59}$$

From this equation we can find the following conditions in order to satisfy $\sigma + \mathcal{P} \geq 0$:

1. For $2M > r_0$:
   (a) If $0 < \beta < 1$, then $2M < a_0 \leq \zeta_3 + \zeta_4$.
   (b) If $\beta < 0$, then $2M < a_0$.

   In order to simplify the analysis of this situation, we shall study the behavior of the surface energy density, tangential surface pressure and NEC with the help of plots made for some particular values of the relevant parameters. This is represented in Fig. 2, where the physical quantities are shown as functions of the junction radius a_0. For simplicity, we consider $M = r_0 = 1$. We shall compare cases with a deficit and excess of solid angle. For $\beta = 1/2$, the NEC is satisfied if the junction radius lies in the range $2 < a_0 < 6.56$. The surface energy density changes sign at $a_0 = 3$, being positive for $a_0 < 3$, while the tangential surface pressure remains always positive, as shown in Fig. 2a. For $\beta = -1/2$, the NEC and surface energy density are always positive, while the tangential surface pressure remains positive if the junction radius lies in the range $2 < a_0 < 4$, as shown in Fig. 2b.
2. For $2M < r_0$:
   (a) If $0 < \beta < 1$:
      i. If $\frac{r_0}{4} < M < \frac{r_0}{3}$:
         A. If $0 < \beta < \frac{(r_0-4M)^2}{(r_0-2M)^2}$, then $\zeta_3 - \zeta_4 \leq a_0 \leq \zeta_3 + \zeta_4$.
         B. If $\beta = \frac{(r_0-4M)^2}{(r_0-2M)^2}$, then $a_0 = \zeta_3 - \zeta_4$.
      ii. If $M = \frac{r_0}{3}$, then $\zeta_3 - \zeta_4 < a_0 \leq \zeta_3 + \zeta_4$.
      iii. If $\frac{r_0}{3} < M < \frac{r_0}{2}$, then $r_0 < a_0 \leq \zeta_3 + \zeta_4$.
   (b) If $\beta < 0$:
      i. If $M < \frac{r_0}{3}$, then $\zeta_3 + \zeta_4 \leq a_0$.
      ii. If $M = \frac{r_0}{3}$, then $\zeta_3 + \zeta_4 < a_0$.
      iii. If $\frac{r_0}{3} < M < \frac{r_0}{2}$, then $r_0 < a_0$.

As we did before, we shall again analyze the behavior of the surface energy density, tangential surface pressure, and NEC with the help of plots made for some particular values of the parameters. This is depicted in Fig. 3. We now consider the parameter values $M = 1$ and $r_0 = 3$. As before, we will compare cases with both a deficit and an excess of solid angle. For $\beta = 1/2$, the surface energy density is consistently nega-

tive, the tangential surface pressure remains positive, and the NEC is satisfied within the range $3 < a_0 < 4$, as shown in Fig. 3a. On the other hand, for $\beta = -1/2$, the energy density becomes positive at $a_0 = 5$, while the tangential pressure remains positive in the range $3 < a_0 < 9.27$. The NEC is satisfied for $3 < a_0$, as shown in Fig. 3b. Thus, there exists an interval for the junction radius a_0, where the surface energy density, the tangential pressure and the NEC are positive.

Let us now perform the analysis of the SEC, which is expressed as $\sigma + \mathcal{P}_{\text{total}} \geq 0$. From this relation, we obtain that:

$$\sigma + 2\mathcal{P} = \frac{M}{8\pi a_0^2\sqrt{1-\frac{2M}{a_0}}}. \tag{60}$$

From this expression, one may directly conclude that the SEC is always satisfied for $2M > a_0$, regardless of the parameter β.

Finally, let us analyze the DEC, which for the surface energy density and the tangential surface pressure may be expressed as:

$$-\sigma \leq \mathcal{P} \leq \sigma. \tag{61}$$

This condition is satisfied in the following cases:

1. For $4M > 3r_0$
   (a) If $0 < \beta < \frac{(4M-3r_0)^2}{9(r0-2M)^2}$, then $\zeta_5 - \zeta_6 \leq a_0 \leq \zeta_5 + \zeta_6$.
   (b) If $\beta = \frac{(4M-3r_0)^2}{9(r0-2M)^2}$, then $a_0 = \zeta_5 + \zeta_6$.
2. For $2M > r0$, if $\beta < 0$, then $\zeta_5 + \zeta_6 < a_0$, where

$$\zeta_5 = \frac{M(4+6\beta) - 3r_0(1-\beta)}{6\beta}, \tag{62}$$

$$\zeta_6 = \frac{1}{6}\sqrt{\frac{(1-\beta)((4M-r_0)^2 - 9(r_0-2M)^2\beta)}{\beta^2}}. \tag{63}$$

In this scenario, we will visualize the behavior of surface energy density and tangential pressure by setting $M = 1$. To consider a situation with a deficit in the solid angle, we set $\beta = 0.1$ and $r_0 = 0.2$. Then the DEC is satisfied if the junction radius lies in the range $2.1 < a_0 < 11.4$, as shown in Fig. 4a. In this scenario, the traversable Schwarzschild-like wormhole takes the form $ds_-^2 = -dt^2 + \frac{dr^2}{\frac{9}{10}\left(1-\frac{1}{r}\right)} + r^2 d\Omega^2$. To consider a situation with an excess in the solid angle, we set $\beta = -1$ and $r_0 = 1$. In this case, the surface energy density and tangential pressure remain positive in the range $2.07 < a_0 < 3$, as shown in Fig. 4b. In this scenario, the interior spacetime, represented by the traversable Schwarzschild-like wormhole, is given by $ds_-^2 = -dt^2 + \frac{dr^2}{2\left(1-\frac{1}{r}\right)} + r^2 d\Omega^2$.

This result is interesting, as for $2M > r_0$, the thin shell may be supported by non-exotic matter, satisfying all energy conditions.

6 Analysis of stability regions of the thin shell

We will study the stability regions of thin shells with positive and negative surface energy densities (49), by considering $\beta \neq 0$ and three cases of redshift functions within the context of the interior metric (45): $\Phi(r) = 0$, $\Phi(r) = r_0/r$, and $\Phi(r) = r/r_0$.

Before delving into the analysis, it is important to highlight some observations derived from the master equation (39), which dictates the stability equilibrium configurations for the specific phantom wormhole geometries:

- It can be shown that for the case $\Phi(r) = 0$, $\eta(a_0) \to -1/2$ when $\beta \to -\infty$ or $a_0 \to \infty$. This indicates that the stability regions are strongly restricted for high values of the solid angle excess as well as large ranges of a_0.
- In the case of $\Phi(r) = r_0/r$, we observe that $\eta(a_0) \to -1/2$ only when $a_0 \to \infty$. This suggests that, in this scenario as well, the stability region is significantly restricted for large values of a_0.

6.1 Positive surface energy density

First, let us consider the case in which the thin shell has a positive surface energy density, i.e. $\sigma(a_0) > 0$ and $m_s(a_0) > 0$. The structure of Eq. (49) leads us to separate the analysis into two cases: $2M > r_0$ and $2M < r_0$.

6.1.1 $2M > r_0$

(i) For $0 < \beta < 1$, the radius a_0 of the thin shell satisfies the following inequality:

$$2M < a_0 < \frac{2M - r_0(1-\beta)}{\beta}. \tag{64}$$

To simplify and clarify the analysis, let us consider specific parameter values. By setting $\beta = 1/2$ and $r_0/M = 1$ in the previous equation, we determine the following condition for the radius a_0:

$$2 < a_0/M < 3. \tag{65}$$

From this inequality, by using Eqs. (51) and (52), we deduce that $m_s(a_0) > 0$ and $\sigma' < 0$. Therefore, the following condition is satisfied:

$$m_s\sigma' < 0. \tag{66}$$

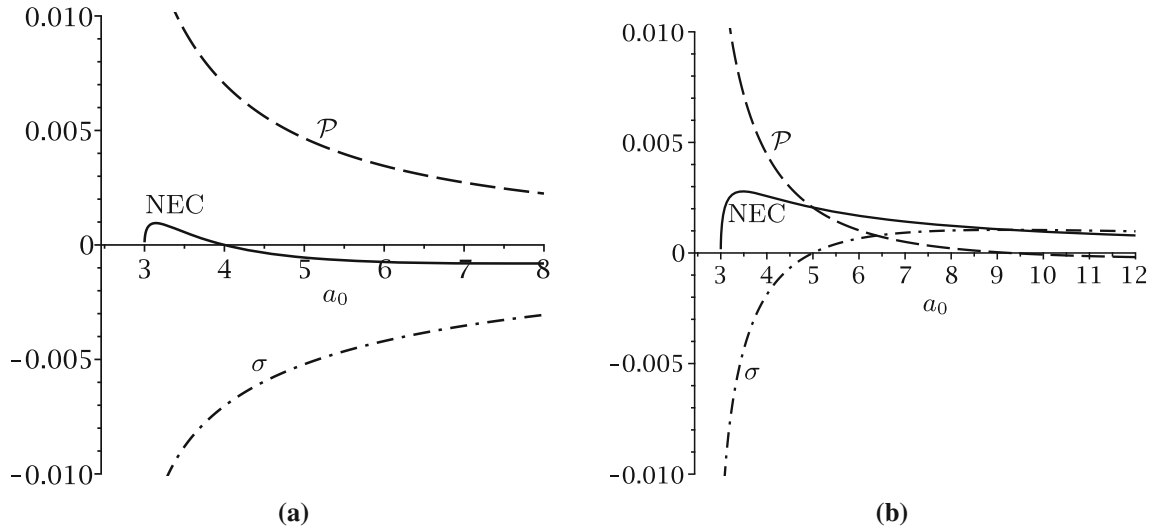

Fig. 3 The behavior of the surface energy density (dash-dot line), surface tangential pressure (dashed line), and NEC (solid line) as functions of the junction radius a_0 is depicted in these plots for the parameter values $2M < r_0$, $\Phi(r) = 0$, $M = 1$, and $r_0 = 3$. Figure (**a**) illustrates the case for $\beta = \frac{1}{2}$, while Figure (**b**) shows the scenario for $\beta = -\frac{1}{2}$. See the main text for details

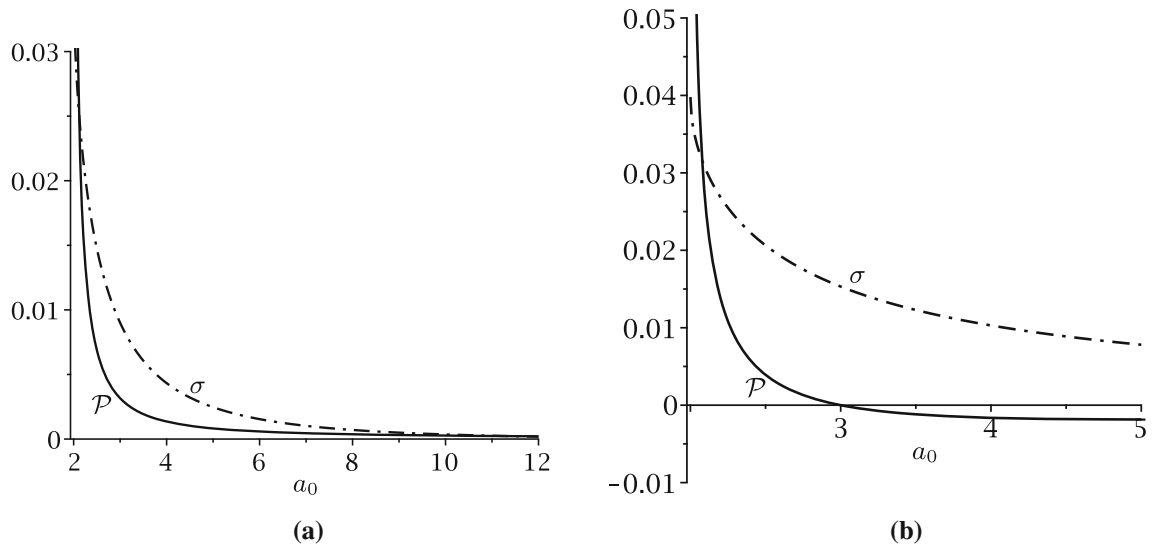

Fig. 4 The plots show the behavior of the surface energy density (dash-dot line) and the surface tangential pressure (dashed line) as functions of the junction radius a_0 in scenarios where the DEC is satisfied, for the parameter values $2M > r_0$ and $\Phi(r) = 0$. Figure (**a**) depicts the case with $M = 1$, $r_0 = 0.2$, and $\beta = 0.1$, while Figure (**b**) illustrates the scenario with $M = r_0 = 1$ and $\beta = -1$. For details, refer to the text

We will now graphically visualize the stability regions of the thin shell for the redshift functions $\Phi(r) = 0$, $\Phi(r) = r_0/r$, and $\Phi(r) = r/r_0$. To do this, we will use the master equation (39). It is important to note that this expression derives from Eqs. (36)–(33), and the effect of the redshift function $\Phi(r)$ is implicitly incorporated in Eq. (38). Therefore, for the inequality (65), using condition (66) and the master equation (39), we conclude that inequality (41) must be satisfied. This allows us to identify that the stability regions lie below the curves of the parameter η_0 shown in Fig. 5a.

Here, it is observed that the stability regions increase when $\Phi(r) \neq 0$, due to the momentum flux (53).

(ii) For $\beta < 0$, we have to fulfill that $a_0 > 2M$. Therefore, the radius of the thin shell is outside the event horizon. By setting $\beta = -2$ and $r_0/M = 1$, we obtain the inequality $2 < a_0/M$. The respective stability regions given by η_0 are shown in Fig. 5b. From Eq. (52), we find that $\sigma' < 0$, and since we are considering a positive surface

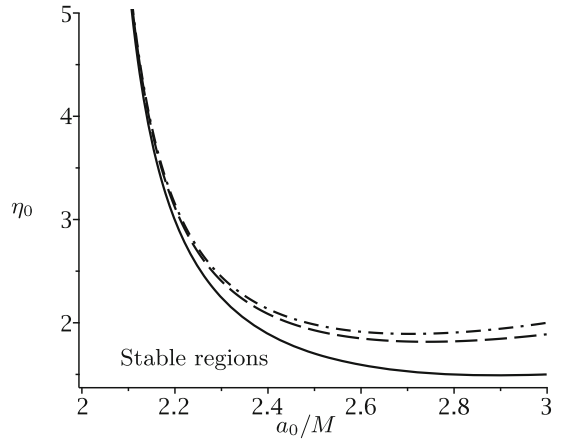

(a)

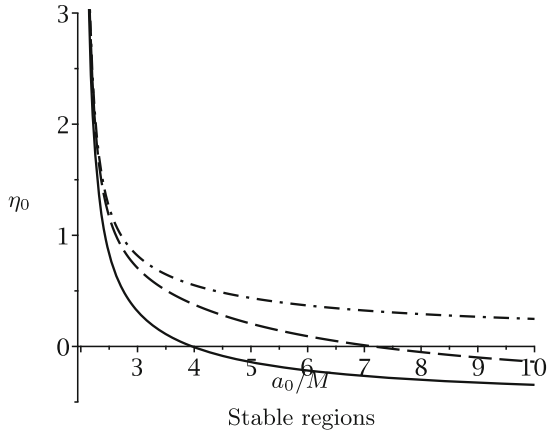

(b)

Fig. 5 The plots show stability regions for cases $\sigma(a_0) > 0$ and $r_0 < 2M$, comparing the redshift functions $\Phi(r) = 0$ (solid line), $\Phi(r) = r_0/r$ (dashed line), and $\Phi(r) = r/r_0$ (dash-dot line). For plot (**a**) with $0 < \beta < 1$, stable equilibrium regions are below the curves. For plot (**b**) $\beta < 0$, stable regions lie below the curves again. In both graphs the zero-tidal solution has the smallest stable region

energy density, this implies $m_s\sigma' < 0$. Therefore, the stability regions, dictated by inequality (41), lie below the η_0 curves. Figure 5b reveals that the stability regions increase for cases where $\Phi(r) \neq 0$. This observation suggests that the introduction of a non-zero function $\Phi(r)$ contributes to enlarging the stability regions of the thin shell.

6.1.2 $2M < r_0$

(i) For $\beta < 0$ and $m_s(a_0) > 0$ we find that:

$$\frac{2M - r_0(1-\beta)}{\beta} < a_0. \tag{67}$$

For this specific case, we can see that the Eq. (52) implies that σ' has a positive real root. Let us denote this root as R, in such a way $\sigma'\big|_R = 0$. This root lies within the range of Eq. (67). This indicates the presence of an asymptote at $\sigma'\big|_R = 0$ (see Fig. 6). We can then verify that $\sigma' > 0$ if $\frac{2M-r_0(1-\beta)}{\beta} < a_0 < R$ and $\sigma' < 0$ if $a_0 > R$. Therefore, the stability regions are restricted by the inequalities:

$$\eta_0 > \Lambda_0, \text{ si, } \frac{2M - r_0(1-\beta)}{\beta} < a_0 < R, \tag{68}$$

$$\eta_0 < \Lambda_0, \text{ si, } a_0 > R. \tag{69}$$

In order to find roots for Eq. (52) we shall impose a relation between r_0 and M. In this way, we will obtain the root R depending on a_0/M. For the particular values $\beta = -2$ and $r_0/M = 2.5$, the asymptote is located at $R = a_0/M = 4.56$, resulting in the inequalities: $2.75 < a_0/M < 4.56$ and $a_0/M > 4.56$. Therefore,

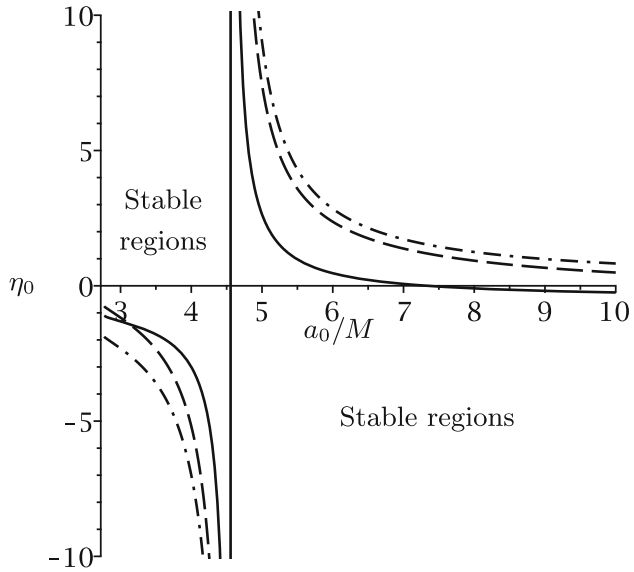

Fig. 6 The figure shows stability regions for $\sigma > 0$, $2M < r_0$ and the redshift functions $\Phi(r) = 0$ (solid line), $\Phi(r) = r_0/r$ (dashed line), and $\Phi(r) = r/r_0$ (dash-dot line). The stable regions to the left of the asymptote at $R = 4.56$ is above the curves and decreases in size in cases with tidal forces. The second stable regions, to the right of the asymptote at $R = 4.56$, is below the curves and increases in size in cases with tidal forces

from inequalities (68) and (69), we conclude that the stability regions are situated above and below the curves of the parameter η_0, as shown and explained in Fig. 6. In comparison with $\Phi(r) = 0$, the stability regions increase for $\Phi(r) \neq 0$.

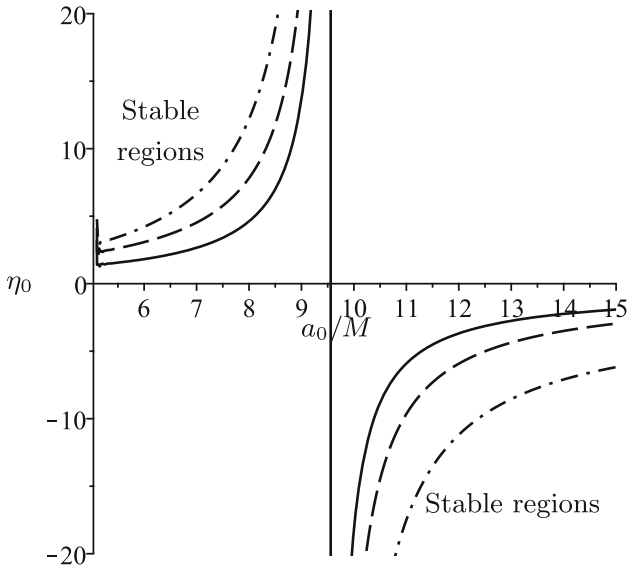

Fig. 7 The graph shows stable equilibrium regions for $\sigma(a_0) < 0$, $r_0 < 2M$ and the redshift functions $\Phi(r) = 0$ (solid line), $\Phi(r) = r_0/r$ (dashed line), and $\Phi(r) = r/r_0$ (dash-dot line). The curves correspond to the case $0 < \beta < 1$, with an asymptote $R = 9.56$. The stable regions to the left of the asymptote at $R = 9.56$ is above the curves and decreases in size in cases with tidal forces. The second stable regions, to the right of the asymptote at $R = 9.56$, is below the curves and decreases in size in cases with tidal forces

6.2 Negative surface energy density

Let us now consider thin shells with a negative surface energy density, i.e. $\sigma(a_0) < 0$ and $m_s(a_0) < 0$. We again consider separately the cases: $2M > r_0$ and $2M < r_0$.

6.2.1 $2M > r_0$

For $0 < \beta < 1$, the radius of the thin shell satisfies the inequation

$$\frac{2M - r_0(1-\beta)}{\beta} < a_0. \tag{70}$$

Using $\sigma'\big|_R = 0$, we find a positive real root R. In order to explicitly showing these regions, we set $r_0/M = 1$ and $\beta = 1/4$, where the root $R = 9.56$. Thus, stable regions are dictated by inequalities $5 < a_0/M < 9.56$ and $9.56 < a_0/M$. In the first interval, we have $\sigma' < 0$, satisfying inequality (40), with stable regions above the curves of η_0 as shown in Fig. 7. Additionally, we observe that η_0 only takes positive values, and the equilibrium region increases for tidal force solutions. In the second interval, we have $\sigma' > 0$, satisfying inequality (41), with stable regions below the curves as shown in Fig. 7. Here, the equilibrium region decreases for tidal force solutions.

6.2.2 $2M < r_0$

(i) For $0 < \beta < 1$, this implies that the thin-shell radius is located in the region

$$r_0 \leq a_0. \tag{71}$$

If we evaluate $r_0/M = 2.4$ then $2.4 < a_0/M$. Then, for $\beta = 1/3$, in this interval we have $\sigma' > 0$, and according to Eq. (41), the stability regions lie below the curves of η_0 as shown in Fig. 8a. Furthermore, it is observed that η_0 takes only negative values, and the equilibrium region for solutions with tidal forces decreases compared to the solution without tidal force, which has the largest stable region.

(ii) For $\beta < 0$, the radius of the thin shell is within the region

$$r_0 \leq a_0 < \frac{2M - r_0(1-\beta)}{\beta}. \tag{72}$$

Evaluating parameters $r_0/M = 3$ and $\beta = -2$, we find $3 < a_0/M < 3.5$. Here, we have $\sigma' > 0$, with stable equilibrium regions lying below the curves of η_0, which are always negative, as shown in Fig. 8b.

7 Conclusions

In this paper, we construct a new thin-shell traversable wormhole using the cut-and-paste procedure and analyze its stability against linearized perturbations around static solutions. One of the advantages of this approach is its simplicity in analyzing stable equilibrium regions of thin shells through a master equation. It should be noted that in the current analysis, the behavior of the mass of the thin shell $m_s(a)$ is linked to the wormhole's stability through manageable inequalities.

The bulk spacetimes on either side of the wormhole thin shell are spherically symmetric and static. Specifically, we consider that the exterior and interior spacetimes are given by Schwarzschild vacuum spacetime and the traversable Schwarzschild-like wormholes, respectively. In the framework of general relativity, both spherically symmetric spacetimes are matched together at a junction spherical surface with an arbitrary radius a_0 and the surface stresses are calculated. In this case the surface stress-energy terms are nonzero, so the junction is not a boundary surface, and it is a thin shell of radius a_0 with a surface mass $m_s = 4\pi a_0^2 \sigma$. All the material is confined to this thin shell. For the exterior Schwarzschild solution, the matching occurs at a junction interface $a_0 > 2M$, situated outside the event horizon, to avoid a black hole solution. This procedure allows for the

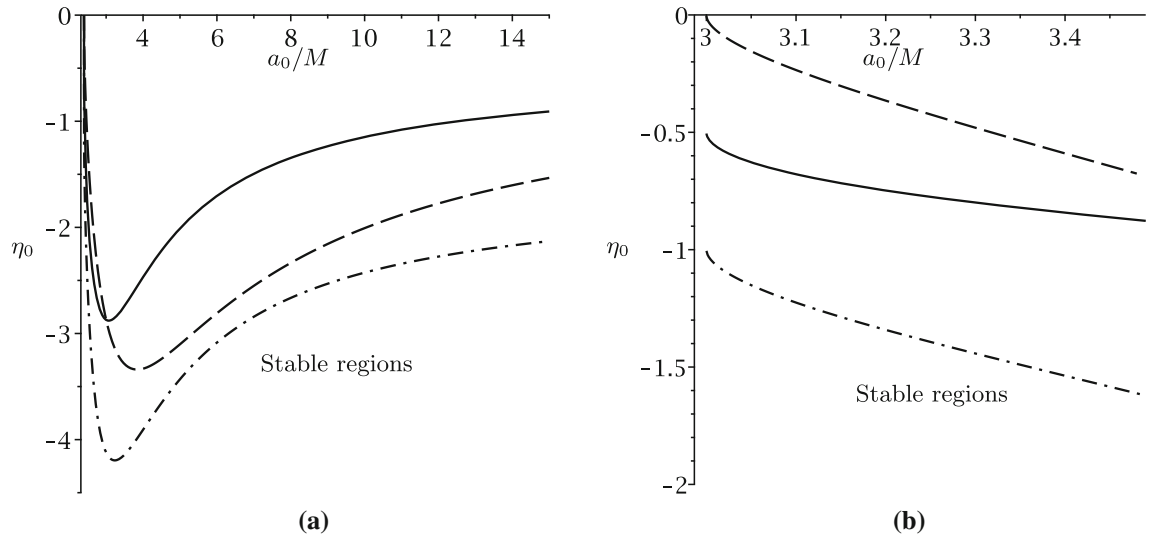

Fig. 8 The graphs show stable equilibrium regions for $\sigma(a_0) < 0$, $2M < r_0$, comparing redshift functions: $\Phi(r) = 0$ (solid line), $\Phi(r) = r_0/r$ (dashed line), and $\Phi(r) = r/r_0$ (dash-dot line). In graph (**a**), for $0 < \beta < 1$, stable regions are below the curves and decrease for tidal force redshift functions. Graph (**b**) corresponds to $\beta < 0$, where stable regions are below the curves. We can see that, $\Phi(r) = r_0/r$ (dashed line) has the largest stable region, while $\Phi(r) = r/r_0$ (dash-dot line) has the smallest stable region

construction of asymptotically flat spacetimes using non-asymptotically flat metrics as interior solutions. Specifically, we use the traversable Schwarzschild-like wormholes constructed in Ref. [24], which are a slight generalization of the traversable Schwarzschild wormhole spacetime, obtained by introducing a linear dependence on the radial coordinate in the shape function.

It can be shown that at spatial infinity, the metric (45) may exhibit a deficit angle for $0 < \beta < 1$ and an excess angle for $\beta < 0$ [24]. The latter case is particularly interesting because the interior solution (45) describes wormholes with a finite size. They extend from the throat to a maximum radius, allowing for the generation of microscopic wormholes.

We perform a stability analysis of this traversable thin-shell wormhole against spherically symmetric perturbations (wormhole stability is related to the properties of the matter residing on the thin-shell) and investigate the behavior of stable equilibrium regions by considering thin shells with both positive and negative surface energy densities, as well as various gravitational redshift functions. It has been found that stable regions depend explicitly on the parameter β. Additionally, the behavior of these stable equilibrium regions can either increase or decrease, depending on the specific form of the gravitational redshift function.

We also analyze the equation of state for the thin shell, given by $\omega = \frac{\mathcal{P}}{\sigma}$. For simplicity, we focus on the zero-tidal-force wormhole solution. We conclude that the thin shell can be supported by dark energy, phantom energy, and, in certain special cases, by non-exotic matter for both $\beta < 0$ and $0 < \beta < 1$, thereby satisfying the dominant energy condition, and consequently also satisfying the weak energy condition and the null energy condition.

Acknowledgements This work was supported by CONICYT-PCHA/Doctorado Nacional/2016 through grant No. 21161114 (LL). MC acknowledges the support of Vicerrectoría de Investigación y Postgrado and Dirección de Investigación y Creación Artística de la Universidad del Bío-Bío through grants No. RE2320220 and No. GI2310339. FO thanks ANID for its support through the grant ANID BECAS/DOCTORADO NACIONAL 21231231.

Funding This work was supported by: - CONICYT-PCHA/Doctorado Nacional/2016 through grant No. 21161114 (LL) - Vicerrectoría de Investigación y Postgrado and Dirección de Investigación y Creación Artística de la Universidad del Bío-Bío through grants No. RE2320220 and No. GI2310339 (MC) - ANID BECAS/DOCTORADO NACIONAL 21231231 (FO).

Data Availability Statement This manuscript has no associated data. [Authors' comment: Data sharing not applicable to this article as no datasets were generated or analysed during the current study.]

Code Availability Statement This manuscript has no associated code/software. [Authors' comment: Code/Software sharing not applicable to this article as no code/software was generated or analysed during the current study.]

Funded by SCOAP[3].

References

1. L. Flamm, Phys. Z **71**, 448 (1916); and republication in Gen. Relativ. Gravit. **47**, 72 (2015). https://doi.org/10.1007/s10714-015-1908-2
2. A. Einstein, N. Rosen, Phys. Rev. **48**, 73 (1935). https://doi.org/10.1103/PhysRev.48.73
3. J.A. Wheeler, Phys. Rev. **97**, 511 (1955). https://doi.org/10.1103/PhysRev.97.511
4. C.W. Misner, J.A. Wheeler, Ann. Phys. **2**, 525 (1957). https://doi.org/10.1016/0003-4916(57)90049-0
5. H.G. Ellis, J. Math. Phys. **14**, 104 (1973). https://doi.org/10.1063/1.1666161
6. M.S. Morris, K.S. Thorne, Am. J. Phys. **56**, 395 (1988). https://doi.org/10.1119/1.15620
7. M.S. Morris, K.S. Thorne, U. Yurtsever, Phys. Rev. Lett. **61**, 1446 (1988). https://doi.org/10.1103/PhysRevLett.61.1446
8. W. Israel, Nuovo Cimento B, **44**, 1 (1966); and corrections in **48**, 463 (1967). https://doi.org/10.1007/BF02710419
9. M. Visser, Nucl. Phys. B **328**, 203 (1989). https://doi.org/10.1016/0550-3213(89)90100-4
10. E. Poisson, M. Visser, Phys. Rev. D **52**, 7318–7321 (1995). https://doi.org/10.1103/PhysRevD.52.7318
11. E. Eiora, C. Simeone, Phys. Rev. D **70**, 044008 (2007). https://doi.org/10.1103/PhysRevD.76.024021
12. J. Lemos, P. Luz, Phys. Rev. D **105**, 044058 (2022). https://doi.org/10.1103/PhysRevD.105.044058
13. M. Ishak, K. Lake, Phys. Rev. D **65**, 044011 (2002). https://doi.org/10.1103/PhysRevD.65.044011
14. F.S.N. Lobo, Phys. Rev. D **71**, 124022 (2005). https://doi.org/10.1103/PhysRevD.71.124022
15. F.S.N. Lobo, P. Crawford, Class. Quantum Gravity **22**, 4869 (2005). https://doi.org/10.1088/0264-9381/22/22/012
16. N. Montelongo Garcia, F.S.N. Lobo, M. Visser, Phys. Rev. D **86**, 044026 (2012). https://doi.org/10.1103/PhysRevD.86.044026
17. E. Eiora, C. Simeone, Phys. Rev. D **70**, 044008 (2004). https://doi.org/10.1103/PhysRevD.70.044008
18. E. Eiora, C. Simeone, Phys. Rev. D **81**, 084022 (2010). https://doi.org/10.1103/PhysRevD.81.084022
19. L.A. Anchordoqui, S. Perez Bergliaffa, D.F. Torres, Phys. Rev. D **55**, 5226 (1997). https://doi.org/10.1103/PhysRevD.55.5226
20. E.F. Eiroa, C. Simeone, Phys. Rev. D **82**, 084039 (2010). https://doi.org/10.1103/PhysRevD.82.084039
21. M.H. Dehghani, M.R. Mehdizadeh, Phys. Rev. D **85**, 024024 (2012). https://doi.org/10.1103/PhysRevD.85.024024
22. I.P. Lobo, M. Graça, J.P. Morais, H. Moradpour, Eur. Phys. J. Plus **135**, 550 (2020). https://doi.org/10.1140/epjp/s13360-020-00553-y
23. A. Khaybullina, G. Tuleganova, Mod. Lett. Phys A **34**, 1950006 (2019). https://doi.org/10.1142/S0217732319500068
24. M. Cataldo, L. Liempi, P. Rodriguez, Eur. Phys. C **77**, 748 (2017). https://doi.org/10.1140/epjc/s10052-017-5332-5
25. E.F. Eiroa, C. Simeone, Phys. Rev. D **81**, 084022 (2010). https://doi.org/10.1103/PhysRevD.81.084022
26. S.D. Forghani, S.H. Mazharimousavi, M. Halilsoy, Phys. Lett. B **804**, 135374 (2020). https://doi.org/10.1016/j.physletb.2020.135374
27. T.W.B. Kibble, J. Phys. A **9**, 1387 (1976). https://doi.org/10.1088/0305-4470/9/8/029
28. A. Vilenkin, E.P.S. Shellard, *Cosmic String and Other Topological Defects* (Cambridge University Press, Cambridge, 1994)
29. T. Vachaspati, https://doi.org/10.48550/arXiv.hep-ph/0101270
30. A.D. Linde, Phys. Lett. B **327**, 208 (1994). https://doi.org/10.1016/0370-2693(94)90719-6
31. J. Pando, D. Valls-Gaboud, L. Fang, Phys. Rev. Lett. **81**, 4568 (1998). https://doi.org/10.1103/PhysRevLett.81.4568
32. U. Nucamendi, M. Salgado, D. Sudarsky, Phys. Rev. Lett. **84**, 3037 (2000). https://doi.org/10.1103/PhysRevLett.84.3037
33. U. Nucamendi, M. Salgado, D. Sudarsky, Phys. Rev. D **63**, 125016 (2001). https://doi.org/10.1103/PhysRevD.63.125016
34. T. Matos, F. Siddharta Guzman, D. Nuñez, Phys. Rev. D **62**, 061301 (2000). https://doi.org/10.1103/PhysRevD.62.061301
35. M. Barriola, A. Vilenkin, Phys. Rev. Lett. **63**, 341 (1989). https://doi.org/10.1103/PhysRevLett.63.341
36. I. Cho, J. Guven, Phys. Rev. D **58**, 063502 (1998). https://doi.org/10.1103/PhysRevD.58.063502
37. J. Spinelly, U. de Freitas, E.R. Bezerra de Mello, Phys. Rev. D **66**, 024018 (2002). https://doi.org/10.1103/PhysRevD.66.024018
38. G. Alencar, M. Nilton, Universe **7**, 332 (2021). https://doi.org/10.3390/universe7090332
39. A.C.L. Santos, C.R. Muniz, L.T. Oliveira, Int. J. Mod. Phys. D **30**, 2150032 (2021). https://doi.org/10.1142/S0218271821500322
40. R. Garanttini, P. Channuie, Nucl. Phys. B **1005**, 116589 (2024). https://doi.org/10.1016/j.nuclphysb.2024.116589